Research Square

Preprints are preliminary reports that have not undergone peer review.
They should not be considered conclusive, used to inform clinical practice,
or referenced by the media as validated information.

Machine Learning-Based Identification of Patients with Elevated Central Venous Pressure Using Features Extracted from Photoplethysmography and Arterial Blood Pressure Waveforms

Ravi Pal
University of California
Walter Rusin
University of California
Akos Rudas
University of California
Jeffrey N. Chiang
University of California
Anna Barney
University of Southampton
Maxime Cannesson
mcannesson@mednet.ucla.edu
University of California

Research Article

Keywords:

Posted Date: November 9th, 2026

DOI: https://doi.org/10.21203/rs.3.rs-10670041/v1

License: This work is licensed under a Creative Commons Attribution 4.0 International License.
Read Full License

Additional Declarations: Competing interest reported. Dr. Cannesson is a consultant for Edwards Lifesciences and Masimo Corp, and has funded research from Edwards Lifesciences and Masimo Corp. He is also the founder of Sironis and Perceptive Medical and he owns patents and receives royalties for closed loop hemodynamic management technologies that have been licensed to Edwards Lifesciences. All the remaining authors declare no conflict of interest.

Machine Learning-Based Identification of Patients with Elevated Central Venous Pressure Using Features Extracted from Photoplethysmography and Arterial Blood Pressure Waveforms

Ravi Pal[1], Walter Rusin[1], Akos Rudas[2], Jeffrey N. Chiang[2], Anna Barney[3], and Maxime Cannesson[1]

[1]Department of Anesthesiology & Perioperative Medicine, University of California, Los Angeles, CA, USA.
[2]Department of Computational Medicine, University of California, Los Angeles, CA, USA.
[3]Institute of Sound and Vibration Research (ISVR), University of Southampton, Southampton, United Kingdom.

Corresponding author: Maxime Cannesson
Email: mcannesson@mednet.ucla.edu

ABSTRACT

Background: Central venous pressure (CVP) is widely used to guide fluid resuscitation and assess right ventricular preload in critically ill and perioperative patients, but requires invasive catheterization associated with procedural risk and resource use. Despite the ubiquity of photoplethysmography (PPG) and arterial blood pressure (ABP) monitoring, their combined use for CVP assessment remains underexplored.

Methods: We investigated whether machine learning (ML) models using features extracted from PPG and ABP waveforms can discriminate between patients with normal and elevated CVP. Using a large perioperative waveform dataset (MLORD, 17,327 surgical patients), we identified 918 patients with concurrent PPG, ABP, and CVP recordings. For each cardiac cycle, a landmark-based feature extraction tool derived 843 PPG and 846 ABP features, spanning time-, frequency-, and morphology-domain characteristics. Cardiac cycle–level features were summarized at the patient level by computing the mean and standard deviation of each PPG and ABP feature. The maximum CVP in each cardiac cycle was also determined and averaged across all cycles to yield a patient-level mean of cycle-level maximum CVP. Patients were classified as having normal CVP (5–15 mmHg) or elevated CVP (>15 mmHg) based on this patient-level mean.

Model development: We evaluated nine ML classifiers-Light Gradient Boosting Machine (LightGBM), eXtreme Gradient Boosting (XGBoost), Random Forest, histogram-based gradient boosting, multilayer perceptron (MLP), k-nearest neighbors (kNN), Gaussian naive Bayes, support vector classifier (SVC), and logistic regression-for binary classification of normal versus elevated CVP. From 3,378 candidate waveform features per patient (1,686 PPG and 1,692 ABP), we selected 91 features using permutation importance constrained by an events-per-variable rule (maximum number of features set to 10% of the total number of patients). Model hyperparameters were tuned using 3-fold grid search on the training set. The optimal configuration for each classifier was then retrained on the full training set (90% of patients; 413 normal, 413 elevated), and performance was evaluated on a held-out test set (10% of patients; 46 normal, 46 elevated). To obtain robust estimates and confidence intervals, we applied a 100-iteration bootstrapping procedure to the test set.

Results: Seven of nine classifiers achieved mean area under the receiver operating characteristic (ROC) curve (AUC) ≥ 0.80 on the test set. Although SVC and XGBoost produced the highest mean AUC and area under the precision–recall curve (AUPRC), LightGBM demonstrated the most balanced overall performance across threshold-dependent metrics at a multi-metric optimized classification threshold. LightGBM achieved a mean AUC of 0.835 (standard deviation 0.042; 95% confidence interval [CI] 0.749–0.916), mean precision 0.827 (0.060; 95% CI 0.727–0.933), mean recall 0.806 (0.054; 95% CI 0.689–0.896), mean F1-score 0.815 (0.043; 95% CI 0.725–0.893), mean AUPRC 0.841 (0.051; 95% CI 0.739–0.938), mean accuracy 0.817 (0.038; 95% CI 0.739–0.891), and mean specificity 0.830 (0.056; 95% CI 0.722–0.931) which was the best overall performance.

Interpretability: We applied SHapley Additive exPlanations (SHAP) to the final LightGBM model to quantify the contribution of individual PPG and ABP features to its predictions. Both PPG and ABP features, including both mean and standard deviation measures, had substantial impact on classification, with top features reflecting venous-influenced diastolic PPG morphology and ABP frequency/morphology characteristics consistent with physiologic ventricular interdependence.

Conclusions: In a large perioperative cohort, combined PPG and ABP waveform features enabled ML-based discrimination between normal and elevated CVP with good performance. These findings suggest that routinely acquired PPG and ABP signals may support minimally invasive screening for elevated CVP and motivate future work on multicenter validation and continuous, noninvasive CVP estimation.

Introduction

In this study, we investigated whether a combination of features derived from photoplethysmography (PPG) and arterial blood pressure (ABP) waveforms can discriminate between patients with normal and elevated central venous pressure (CVP) using machine learning (ML). CVP measurement is widely used in operating rooms and intensive care units to estimate the body's need for fluids in patients with hemodynamic instability [1-3]. A CVP range of 5-15 mmHg is generally considered normal [4]. CVP is regarded as a reliable indicator of right ventricular preload, used to assess cardiac preload and volume status, and supports the diagnosis of right-sided heart failure [5,6]. Elevated CVP is often associated with organ dysfunction [7] and may reflect impaired right ventricular filling due to reduced ventricular compliance [8]. CVP is typically measured by inserting a catheter into the superior vena cava via the internal jugular vein or subclavian vein [3]. However, this invasive approach is time-consuming and carries inherent significant procedural risks - including pneumothorax, vascular injury, and catheter-related bloodstream infection - and requires a skilled operator to perform safely [9,10]. We therefore hypothesize that the PPG and ABP waveforms, which carry abundant clinically important physiological information crucial for diagnosing and monitoring patients' health [11-14], have potential as less invasive alternatives to direct CVP measurement.

PPG is a non-invasive, standard-of-care signal already embedded in routine clinical practice, most commonly used to measure blood oxygen saturation via pulse oximetry [11,15]. The richness of physiological information encoded in the PPG waveform, combined with the simplicity and low cost of its acquisition, has driven a rapid expansion of its clinical and consumer applications. PPG has been used to estimate blood pressure, detect atrial fibrillation, screen for diabetes, assess vascular aging, identify sleep-disordered breathing (including apnea and hypopnea), infer emotional and autonomic states, and estimate cardiac output [11,16]. More recently, advances in digital signal processing and ML have accelerated the integration of PPG analysis into consumer wearables such as smartwatches and fitness trackers [17-19]. The convergence of signal processing and ML has opened new avenues for extracting clinically meaningful information from PPG, extending its utility from continuous heart-rate tracking to more sophisticated forms of everyday physiological monitoring [18,20].

Within this broader context, PPG has also emerged as a candidate modality for CVP assessment. Prior work has shown that morphological variations in the peripheral PPG waveform can reflect venous pulsations modulated by CVP, especially at higher CVPs [21-26] . More directly, reflectance-mode contact PPG applied to the anterior neck has demonstrated the ability to capture the jugular venous pressure waveform, offering a non-invasive route to CVP estimation [27]. Despite these findings and PPG's widespread availability, its application for CVP assessment remains comparatively underexplored relative to its other physiological uses.

Similar to PPG, the ABP waveform also contains rich morphological information beyond its established role in continuous blood pressure monitoring. ABP features - such as upstroke slope, dicrotic notch characteristics, and pulse pressure variation - have long been used clinically to infer stroke volume, arterial compliance, and fluid responsiveness [28–30]. Respiratory-induced variations in the ABP waveform, including pulse pressure variation (PPV) and stroke volume variation (SVV), are established surrogates of preload dependency and are routinely used to guide fluid management in mechanically ventilated patients [31]. Given the physiological interdependence between right and left heart filling, elevations in CVP may subtly influence left ventricular preload and, in turn, the morphology of the arterial waveform [32-34].

Our pilot work indicated that both PPG and ABP waveforms had some potential as predictors of CVP, but that neither alone could identify elevated CVP with sufficient confidence for clinical use. We propose that because ABP and PPG arise from the same underlying cardiac cycle, their combined analysis may reveal complementary information not evident in either signal on its own [35].

Although arterial lines are invasive compared to PPG sensors they are also already standard of care in many patients for whom CVP assessment is most relevant, Arterial line placement is generally faster, requires less specialized training, and carries a more favorable complication profile than central venous catheterization, with risks largely limited to distal ischemia and hematoma rather than the more severe pneumothorax, hemothorax, or infection associated with central access [36,37]. Moreover, because arterial lines are frequently placed for indications independent of CVP monitoring - such as continuous blood pressure surveillance or frequent arterial blood gas sampling - leveraging the existing ABP waveform for CVP estimation introduces no additional procedural risk in patients who already have arterial access in place. In this sense combining PPG and ABP features represents a pragmatic compromise along the invasiveness-information spectrum: fully non-invasive PPG alone may lack sufficient signal to reliably capture central hemodynamics, whereas central venous catheterization provides the richest information, but at the highest procedural risk; ABP, as a minimally invasive but ubiquitous signal, may help bridge the gap without requiring additional instrumentation or risk exposure.

Despite the richness of physiological information encoded in PPG and ABP waveforms and prior work demonstrating that

venous pulsations can influence PPG morphology, the combined use of these signals for CVP assessment has not been systematically evaluated in a large perioperative cohort. Existing studies of PPG-based CVP estimation have been limited by small sample sizes, narrow clinical contexts, and a lack of feature-level interpretability. Moreover, few investigations have explored how ABP waveform features, which arise from the same cardiac cycle and reflect left-sided hemodynamics, might complement PPG in characterizing elevations in CVP.

In this study, we focused on patient-level classification rather than continuous CVP waveform estimation, reasoning that identifying patients with persistently elevated CVP may have direct implications for fluid management and hemodynamic monitoring in perioperative care. We applied our recently developed feature extraction tool [38,39] to derive features from both PPG and ABP waveforms. Using the combined feature set, we trained nine different ML classifiers - Light Gradient Boosting Machine (LightGBM) [40], eXtreme Gradient Boosting (XGBoost) [41], Random Forest [42], histogram-based gradient boosting [43], multilayer perceptron (MLP) [44], k-nearest neighbors (kNN) [45] (with k=10), Gaussian Naive Bayes [46], support vector classifier (SVC) [47], and logistic regression [48] - to differentiate between patients with normal and elevated CVP. These classifiers were selected based on their widespread use in physiological waveform-based classification tasks, including those involving PPG and ABP waveforms [49-52]. Additionally, we employed SHapley Additive exPlanations (SHAP) [53] to interpret the predictions of the best-performing model. SHAP analysis quantifies how much each input feature (in our study, a PPG or ABP feature) contributes to the model's output [54]. While this study does not directly estimate the CVP waveform from the PPG and ABP signals, it lays the groundwork for future research into less invasive and more widely accessible approaches to CVP assessment.

The key contributions of this work are:

1. Evaluation of nine ML classifiers using a combination of time-, frequency-, and morphology-domain features derived from PPG and ABP waveforms to identify patients with elevated CVP in a large, perioperative dataset of 918 patients.
2. Rigorous performance assessment using 3-fold cross-validation with grid search on the training set, model-specific threshold optimization, and bootstrap-derived confidence intervals on an independent test set to quantify the robustness of classification.
3. Application of an explainable AI approach, SHAP, to the best-performing model (LightGBM) to characterize the relative importance and physiological interpretation of individual PPG and ABP features in distinguishing normal from elevated CVP.

Methods

Previous studies have shown that the morphology of the PPG waveform can be influenced by venous pressure [21,24,27], with the diastolic phase of the PPG signal particularly amplified by the venous component [21,24]. Accordingly, PPG waveforms recorded under normal versus elevated CVP conditions may exhibit distinct morphological differences, especially during the diastole. For example, Fig. 1(i-a) and Fig. 1(ii-a) illustrate diastolic-phase differences in the PPG cardiac cycles corresponding to

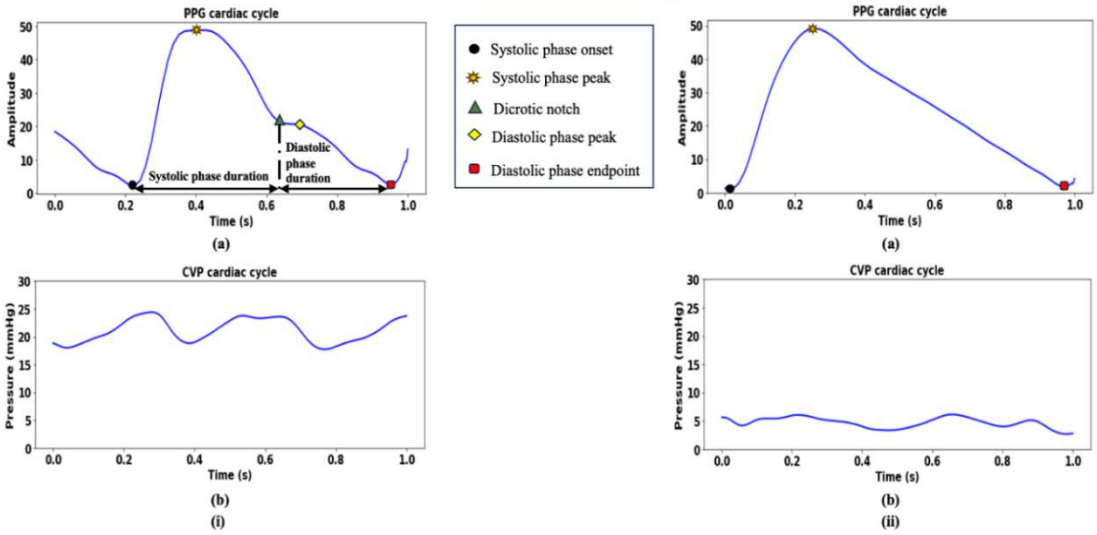


Fig. 1. (i) Photoplethysmography (PPG) cardiac cycle with all five key landmarks (a) and the corresponding central venous pressure (CVP) cardiac cycle with high CVP (b); and (ii) PPG cardiac cycle with only three key landmarks visible (a) and the corresponding CVP cardiac cycle with normal CVP (b).

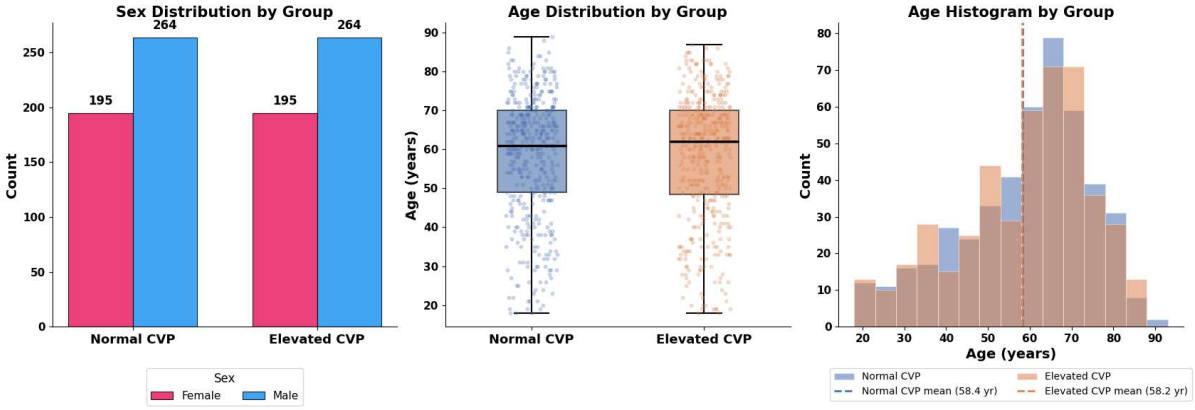


Fig. 2. Age and sex distribution in normal and elevated central venous pressure patient groups.

the high-and normal-CVP cycles shown in Fig. 1(i-b) and Fig. 1(ii-b), respectively. Although such differences are not always obvious in the raw waveform, advanced signal-processing-based feature extraction can capture clinically meaningful characteristics from PPG signals. In addition, features derived from the ABP waveform may provide complementary information. Therefore, combining PPG and ABP features within an ML model could play a valuable role in identifying patients with elevated CVP.

Dataset

We used the large perioperative dataset (MLORD), which contains physiological waveforms from 17,327 patients who underwent surgery between 2019 and 2022 at the David Geffen School of Medicine, University of California Los Angeles (IRB# 19–000354; NIH research funding: R01HL14469) [55], to evaluate the performance of the ML models. MLORD includes both clinical and physiological waveform recordings. Clinical data were extracted from the electronic health record (EHR) systems Epic (Verona, WI, USA) and Surgical Information Systems (Alpharetta, GA, USA), and waveform data were captured in the operating rooms using the Bernoulli data acquisition system (Cardiopulmonary, New Haven, CT, USA).

In total, the waveform repository comprises more than 72,264 hours of recordings (approximately 7.6 TB) of digital physiological signals, including electrocardiograms (ECG), ABP, PPG, and CVP [55]. For this study, we analyzed a subset of 918 patients with concurrent PPG, ABP, and CVP recordings, evenly divided between the normal CVP group and the elevated CVP group (459 patients each), with groups matched for age and sex. The age and sex distribution of the two groups is shown in Fig. 2. All waveforms were sampled at 256 Hz.

Waveform Feature Extraction

We used a recently developed signal processing-based feature extraction tool for extracting features from PPG and ABP waveforms [39]. The tool operates in two steps: first, it identifies all key landmarks within a cardiac cycle - systolic phase onset, systolic peak, dicrotic notch, diastolic peak, and diastolic phase endpoint – as illustrated in Figure 1(i-a); second, it uses these landmarks, to compute more than 840 features per cycle. We selected this tool for PPG and ABP waveforms featurization for two main reasons: (1) its high accuracy in detecting key landmarks, even when they are less visible in the input signal, and (2) its ability to generate a large set of candidate features whose clinical usability can be systematically evaluated. In this study, the tool extracted 843 PPG features and 846 ABP features per cardiac cycle (CC) from the PPG and ABP waveforms, respectively, encompassing time-domain, frequency-domain, and statistical characteristics. Separately, from the CVP waveform, the maximum value corresponding to each cardiac cycle was determined. Cardiac cycle-level features were then summarized at the patient level by calculating the mean and standard deviation of each PPG and ABP feature across all cycles, yielding 843 mean PPG features, 843 PPG feature standard deviations, 846 mean ABP features, and 846 ABP feature standard deviations per each patient. The maximum CVP values were likewise averaged across all cardiac cycles to obtain a single patient-level mean maximum CVP value. For a detailed explanation of the feature extraction tool and the full set of PPG features, we refer readers to our previous work [38,39].

Models development

To prepare the dataset, we divided the 918 patients into training and test subsets. In clinical practice, a CVP range of 5–15 mmHg is generally considered normal [4]. Accordingly, patients with a patient-level mean of cycle-level maximum CVP between 5 and 15 mmHg were classified as having normal CVP, and those with values >15 mmHg were classified as having elevated CVP.

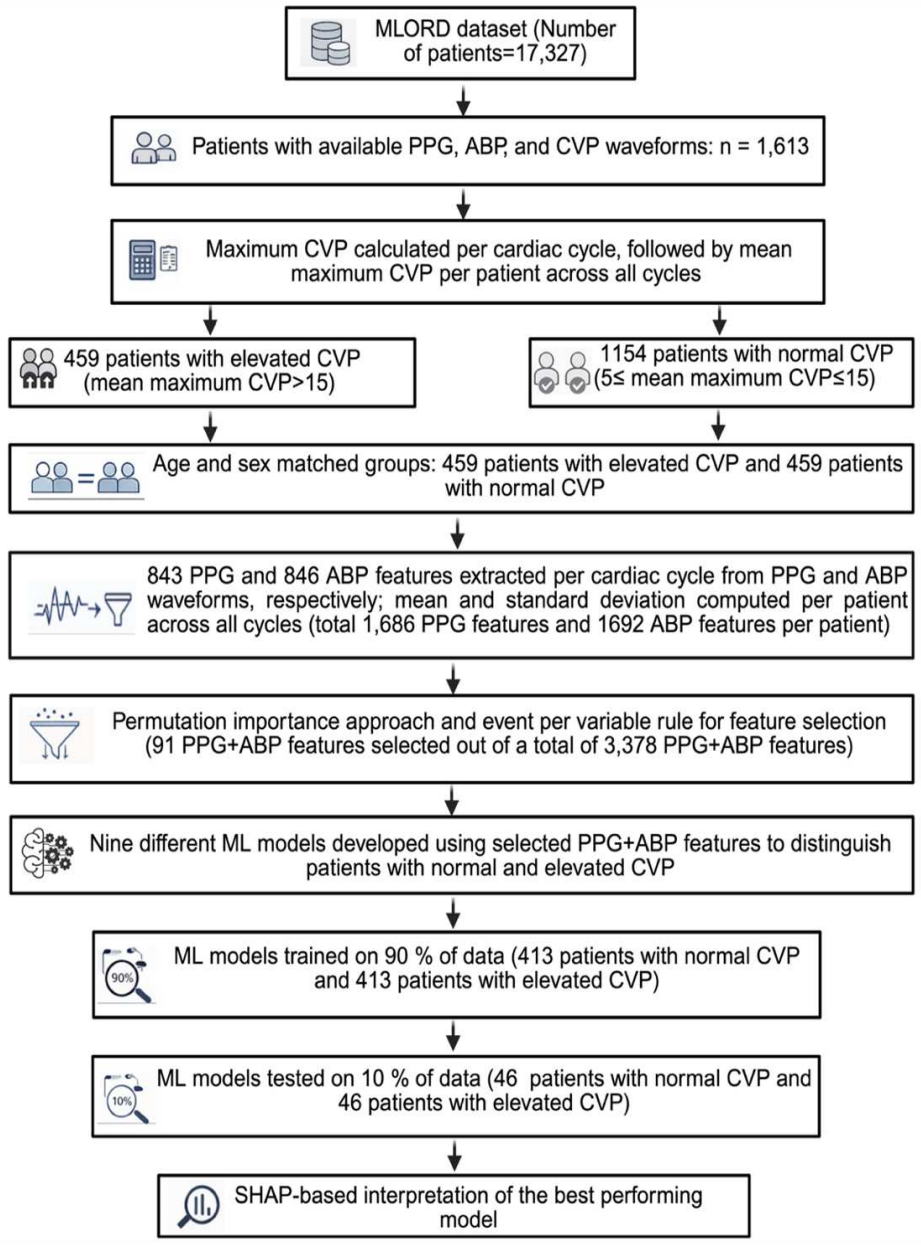


Fig. 3. Block diagram of the workflow used in this study using the MLORD dataset.

The cohort was evenly split between normal and elevated groups (459 patients each) of whom 90% (413 normal, 413 elevated) were allocated to the training set and 10% (46 normal, 46 elevated) to an independent test set. Feature selection was performed on the training data set using a permutation importance approach [56] combined with the events-per-variable rule [57], yielding 91 informative features from a total of 1,686 PPG features (843 mean and 843 standard deviation features) and 1,692 ABP features (846 mean and 846 standard deviation features). Permutation importance scores were computed on the training data and used to rank all features; to prevent overfitting, control computational complexity, and improve generalizability, we then retained only the top-ranked features, limiting the maximum number of selected features set to 10% of the total number of patients, in accordance with the event-per-variable rule. Using the selected PPG and ABP waveform features, we developed multiple ML models, including logistic regression, LightGBM, XGBoost, Random Forest, histogram-based gradient boosting, multilayer perceptron (MLP), k-nearest neighbors (kNN), support vector classifier (SVC), and Gaussian Naive Bayes. For each model hyperparameters were tuned using 3-fold grid search on the training set to identify the optimal configuration, after which the best-performing settings were retrained on the full training set and evaluated on the held-out test set. The optimal hyperparameter combination for each ML model is presented in Table 1. All models were developed using the Python programming language (version 3.12.2). LightGBM and XGBoost were implemented using their respective standalone Python libraries, whereas the remaining models were implemented using the Scikit-learn library.

Table 1. Hyperparameter settings for classifiers.

Classifier	Parameter
LightGBM	learning_rate= 0.2 max_depth= 5 n_estimators= 500 num_leaves= 20
XGBoost	learning_rate= 0.05 max_depth= 3 n_estimators= 200
Random Forest	max_depth= 10 min_samples_split= 5 n_estimators= 100
Histogram-Based Gradient Boosting	learning_rate= 0.1 max_depth= 5 max_iter= 200
Logistic Regression	Cost= 0.01
kNN	metric= Euclidean n_neighbors= 10 weights= distance
SVC	Cost= 1 kernel= rbf
MLP	alpha= 0.001 hidden_layer_sizes= (100,) learning_rate_init= 0.001
Gaussian Naive Bayes	var_smoothing= 1e-12

Model evaluation

The performance of the ML models for identifying patients with elevated CVP was evaluated using the area under the receiver operating characteristic curve (AUROC), area under the precision recall curve (AUPRC), precision (positive predictive value), recall (sensitivity), F1-score, accuracy, and specificity [58,59]. AUROC and AUPRC are widely used discrimination metrics for assessing classification performance. Precision measures the proportion of patients predicted by the model to have elevated CVP who are true positives, whereas recall measures the proportion of true elevated CVP patients correctly identified by the model. The F1-score, defined as the harmonic mean of precision and recall, provides a single summary of the balance between these two metrics. Accuracy is the ratio of correctly classified patients to the total number of patients in the test set, and specificity, denotes the proportion of true normal-CVP patients correctly identified by the model. Threshold-dependent metrics were computed at a model-specific, multi-metric optimized threshold chosen to minimize the standard deviation of accuracy, sensitivity, precision, and specificity, thereby encouraging balanced performance across metrics. To further ensure robustness, we applied a 100-iteration bootstrapping procedure to the test set to estimate performance metrics and their corresponding 95% confidence intervals [60].

Interpretability analyses

We applied SHapley Additive exPlanations (SHAP) method [53] to the model with the best overall performance to quantify the contribution of individual PPG and ABP feature to its predictions. SHAP is a widely used feature-level interpretability technique that can be integrated into ML models to improve transparency, trust, and understanding of their outputs [61]. Its core principle is to assign a Shapley value to each feature, representing that feature's contribution to the model's prediction for a given data point [54]. SHAP analysis was performed using the Python SHAP package [62]. For clarity, Fig. 3 presents a block diagram of the complete workflow used in this study.

Results

Models Performance

On the held-out test set, seven of the nine evaluated ML classifiers achieved mean AUROC values ≥0.80, whereas logistic regression and kNN achieved mean AUROCs of 0.79 and 0.71, respectively. Although, SVC and XGBoost yielded the highest mean AUROC and AUPRC, the LightGBM classifier demonstrated the most balanced overall performance in distinguishing patients with elevated CVP from those with normal CVP at a model-specific, multi-metric optimized threshold (Fig. 4). LightGBM achieved a mean AUROC of 0.835 (SD 0.042; 95% CI: 0.749–0.916), mean precision 0.827 (SD 0.060; 95% CI: 0.727-0.933), mean recall 0.806 (SD 0.054; 95% CI: 0.689-0.896), mean F1-score 0.815 (SD 0.043; 95% CI: 0.725-0.893), mean AUPRC 0.841 (SD 0.051; 95% CI: 0.739-0.938), mean accuracy 0.817 (SD 0.038; 95% CI: 0.739-0.891), and a mean specificity

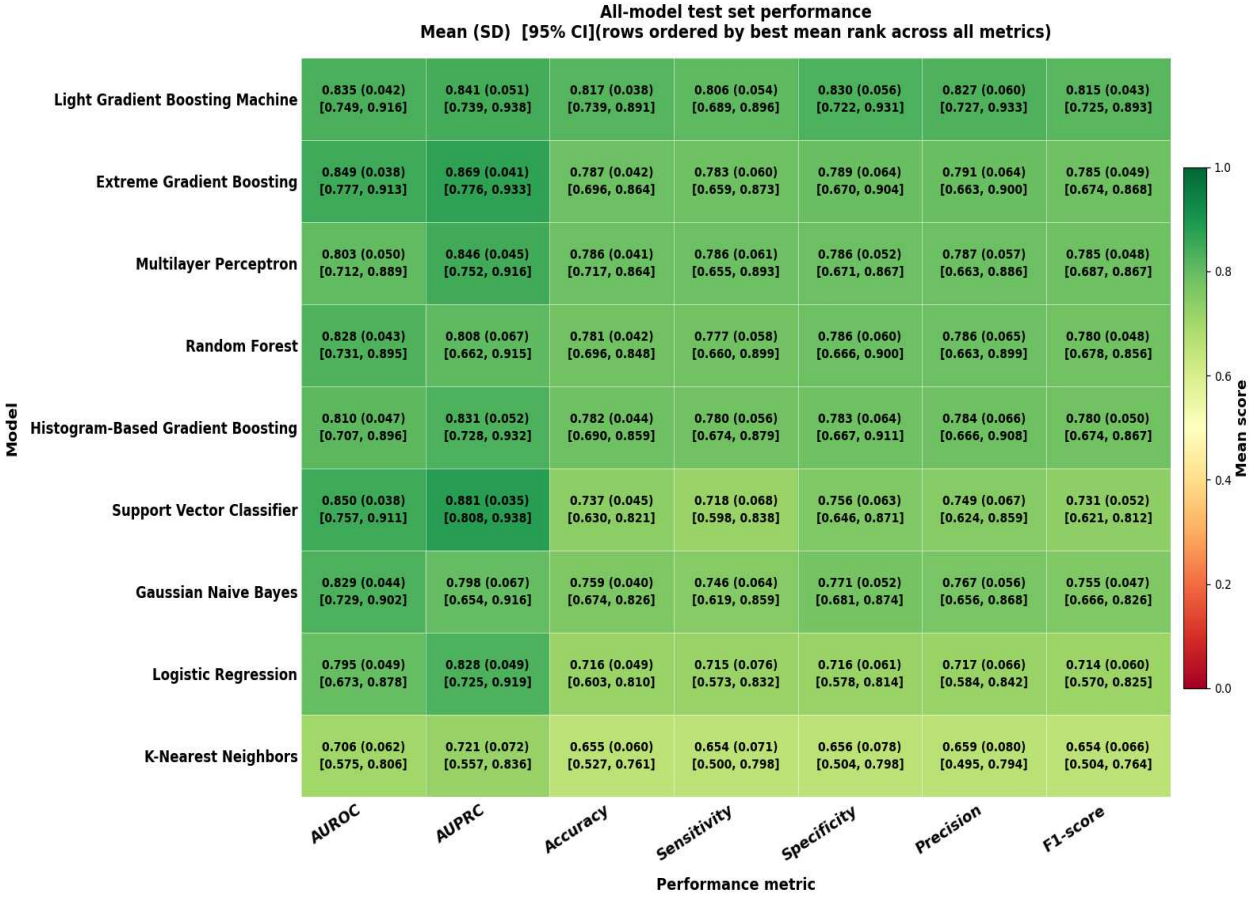


Fig. 4. Comparative performance of evaluated models on the held-out test set. Heatmap showing area under the receiver operating characteristic (AUROC) curve, area under the precision recall curve (AUPRC), accuracy, sensitivity, specificity, precision, and F1-score for each model. Threshold-dependent metrics were evaluated at model-specific multi-metric optimized threshold (minimum standard deviation of accuracy, sensitivity, precision, and specificity) to achieve balanced performance across metrics. Models are ordered from top to bottom by ascending mean rank across all seven-performance metrics, such that the highest overall-performing model appears at the top. Color intensity represents metric value, ranging from low (red) to high (green). SD: standard deviation. CI: confidence interval.

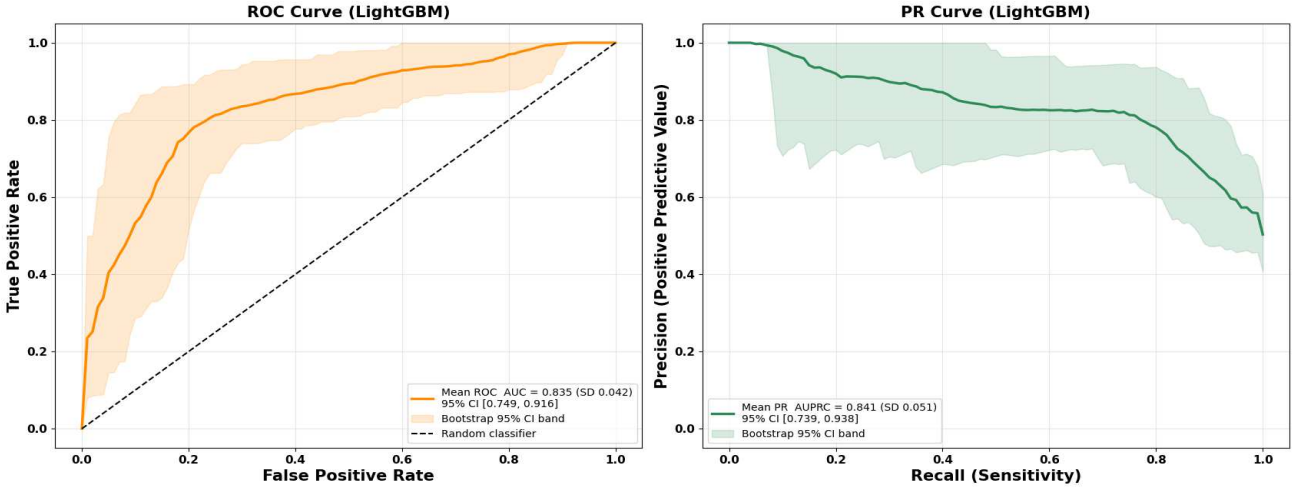
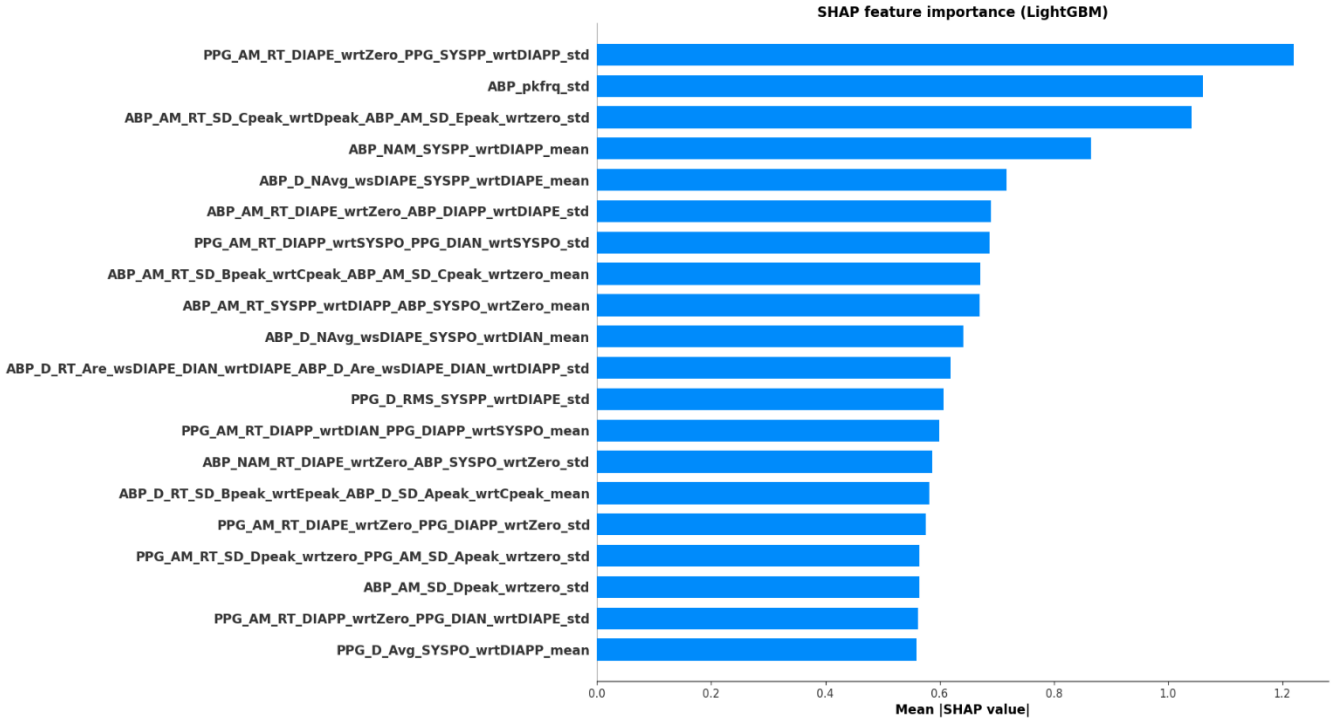
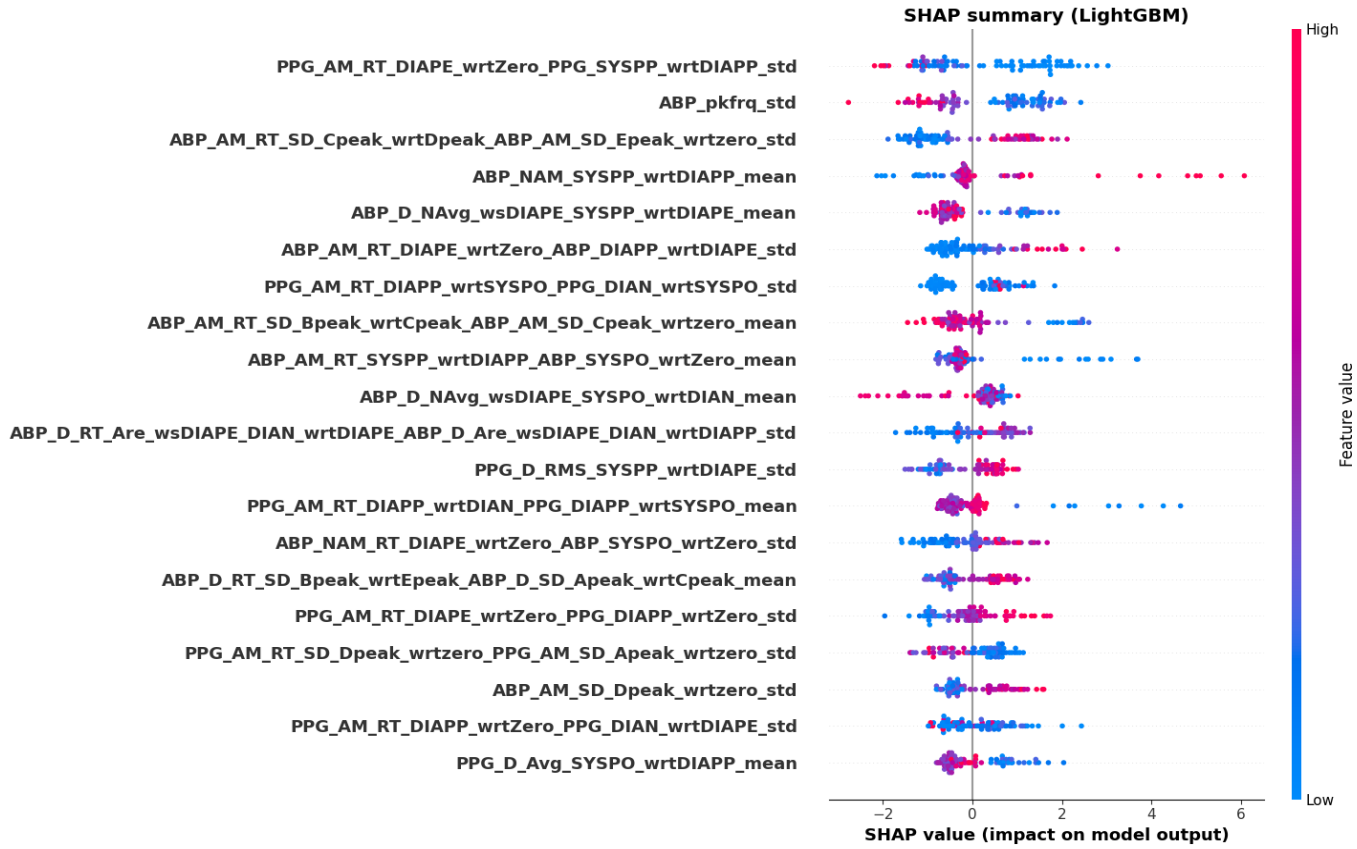


Fig. 5. (a) Receiver operating characteristic (ROC) curve and (b) precision-recall curve for the LightGBM model, which demonstrated the most balanced overall performance among all evaluated models. SD: standard deviation; CI: confidence interval.

0.830 (SD 0.056; 95% CI: 0.722-0.931). For the LightGBM model, all threshold-dependent metrics were evaluated using a classification threshold of 0.7013. Standard deviations are reported alongside means for all performance metrics. The mean ROC and precision-recall curves for LightGBM, together with their corresponding 95% confidence intervals, are shown in Fig. 5(a) and Fig. 5(b), respectively.



(a)



(b)

Fig. 6. (a) SHAP feature importance bar plot of the top 20 features from the combined PPG and ABP feature set in the LightGBM model; (b) SHAP summary plot of these top 20 features. Features are ranked in descending order of importance in the model.

Table 2. Detailed descriptions of the top 20 most important ABP+PPG features that contributed to the ML model prediction (Fig. 6).

	Feature	Description
1	PPG_AM_RT_DIAPE_wrtZero_PPG_SYSPP_wrtDIAPP_std	Standard deviation across cardiac cycles of the ratio of the PPG cardiac cycle diastolic phase end point with respect to zero to the PPG cardiac cycle systolic phase peak amplitude with respect to diastolic phase peak
2	ABP_pkfrq_std	Standard deviation across cardiac cycles of the frequency corresponding to the first peak in the FFT of the ABP cardiac cycle
3	ABP_AM_RT_SD_Cpeak_wrtDpeak_ABP_AM_SD_Epeak_wrtzero_std	Standard deviation across cardiac cycles of the ratio of the ABP cardiac cycle second derivative Cpeak amplitude with respect to Dpeak to the ABP cardiac cycle second derivative Epeak amplitude with respect to zero
4	ABP_NAM_SYSPP_wrtDIAPP_mean	Mean across cardiac cycles of the normalized ABP cardiac cycle systolic phase peak amplitude with respect to diastolic phase peak
5	ABP_D_NAvg_wsDIAPE_SYSPP_wrtDIAPE_mean	Mean across cardiac cycles of the average duration of the normalized ABP cardiac cycle systolic phase peak with respect to diastolic phase end point, with subtracted diastolic phase end point
6	ABP_AM_RT_DIAPE_wrtZero_ABP_DIAPP_wrtDIAPE_std	Standard deviation across cardiac cycles of the ratio of the ABP cardiac cycle diastolic phase end point amplitude with respect to zero to the ABP cardiac cycle diastolic phase peak amplitude with respect to diastolic phase end point
7	PPG_AM_RT_DIAPP_wrtSYSPO_PPG_DIAN_wrtSYSPO_std	Standard deviation across cardiac cycles of the ratio of the PPG cardiac cycle diastolic phase peak amplitude with respect to systolic phase onset to the PPG cardiac cycle dicrotic notch amplitude with respect to systolic phase onset
8	ABP_AM_RT_SD_Bpeak_wrtCpeak_ABP_AM_SD_Cpeak_wrtzero_mean	Mean across cardiac cycles of the ratio of the ABP cardiac cycle second derivative Bpeak amplitude with respect to Cpeak to the ABP cardiac cycle second derivative Cpeak amplitude with respect to zero
9	ABP_AM_RT_SYSPP_wrtDIAPP_ABP_SYSPO_wrtZero_mean	Mean across cardiac cycles of the ratio of the ABP cardiac cycle systolic phase peak amplitude with respect to diastolic phase peak to the ABP cardiac cycle systolic phase onset amplitude with respect to zero
10	ABP_D_NAvg_wsDIAPE_SYSPO_wrtDIAN_mean	Mean across cardiac cycles of the average duration of the normalized ABP cardiac cycle systolic phase onset with respect to dicrotic notch, with subtracted diastolic phase end point
11	ABP_D_RT_Are_wsDIAPE_DIAN_wrtDIAPE_ABP_D_Are_wsDIAPE_DIAN_wrtDIAPP_std	Standard deviation across cardiac cycles of the ratio of the area under the ABP cardiac cycle dicrotic notch with respect to diastolic phase end point, with subtracted diastolic phase end point to the area under the ABP cardiac cycle dicrotic notch with respect to diastolic phase peak, with subtracted diastolic phase end point
12	PPG_D_RMS_SYSPP_wrtDIAPE_std	Standard deviation across cardiac cycles of the root mean square duration of the PPG cardiac cycle systolic phase peak with respect to diastolic phase end point
13	PPG_AM_RT_DIAPP_wrtDIAN_PPG_DIAPP_wrtSYSPO_mean	Mean across cardiac cycles of the ratio of the PPG cardiac cycle diastolic phase peak amplitude with respect to dicrotic notch to the PPG cardiac cycle diastolic phase peak with respect to systolic phase onset
14	ABP_NAM_RT_DIAPE_wrtZero_ABP_SYSPO_wrtZero_std	Standard deviation across cardiac cycles of the ratio of the normalized ABP cardiac cycle diastolic phase end point with respect to zero to the normalized ABP cardiac cycle systolic phase onset amplitude with respect to zero
15	ABP_D_RT_SD_Bpeak_wrtEpeak_ABP_D_SD_Apeak_wrtCpeak_mean	Mean across cardiac cycles of the ratio of the ABP cardiac cycle second derivative Bpeak duration with respect to Epeak to the ABP cardiac cycle second derivative Apeak duration with respect to Cpeak
16	PPG_AM_RT_DIAPE_wrtZero_PPG_DIAPP_wrtZero_std	Standard deviation across cardiac cycles of the ratio of the PPG cardiac cycle diastolic phase end point amplitude with respect to zero to the PPG cardiac cycle diastolic phase peak amplitude with respect to zero
17	PPG_AM_RT_SD_Dpeak_wrtzero_PPG_AM_SD_Apeak_wrtzero_std	Standard deviation across cardiac cycles of the ratio of the PPG cardiac cycle second derivative Dpeak amplitude with respect to zero to the PPG cardiac cycle second derivative Apeak amplitude with respect to zero
18	ABP_AM_SD_Dpeak_wrtzero_std	Standard deviation across cardiac cycles of the ABP cardiac cycle second derivative Dpeak amplitude with respect to zero
19	PPG_AM_RT_DIAPP_wrtZero_PPG_DIAN_wrtDIAPE_std	Standard deviation across cardiac cycles of the ratio of the PPG cardiac cycle diastolic phase peak amplitude with respect to zero to the PPG cardiac cycle dicrotic notch amplitude with respect to diastolic phase end point
20	PPG_D_Avg_SYSPO_wrtDIAPP_mean	Mean across cardiac cycles of the average duration of the PPG cardiac cycle systolic phase onset with respect to diastolic phase peak

PPG: Photoplethysmography, ABP: Arterial Blood Pressure; FFT: Fast Fourier Transform. _mean: mean across cardiac cycles for each subject; _std: standard deviation across cardiac cycles for each subject.

SHAP method to explain the LightGBM classifications

We used SHAP to quantify the contribution of individual PPG and ABP features to the predictions of the LightGBM model, which provided the best overall classification performance. Fig. 6(a) shows the SHAP feature-importance bar plot, listing the top 20 features in descending order, with higher positions on the y-axis indicating greater influence on model output. The most influential features are a mix of those derived from PPG and from ABP indicating that both waveforms play a role in the classification process. Fig. 6(b) presents the SHAP summary plot, which displays the distribution of SHAP values for these features across all samples and highlighting both the magnitude and direction of their effects on predictions. In this plot, positive SHAP values indicate increased risk of elevated CVP, whereas negative values suggest decreased risk. Each point represents an individual sample, and colour encodes the corresponding feature value, with high values shown in red and low values in blue, thereby illustrating how variation in feature values shapes the model's output. A detailed description of the top 20 features,

including features derived from both PPG and ABP waveforms, is provided in Table 2.

SHAP analysis indicated that several PPG and ABP features, including both mean and standard deviation measures, exerted a substantial influence on model predictions. Notable examples include the standard deviation of the ratio of the PPG cardiac cycle diastolic phase end point (with respect to zero) to the PPG systolic peak amplitude (with respect to the diastolic peak), the standard deviation of the frequency corresponding to the first peak in the Fast Fourier Transform (FFT) of the ABP cardiac cycle, the standard deviation of the ratio of the ABP cardiac cycle second derivative C-peak amplitude (with respect to D-peak) to the second derivative E-peak amplitude (with respect to zero), the mean of the normalized ABP systolic peak (with respect to diastolic peak), and the mean duration of the normalized ABP systolic peak (with respect to diastolic phase end point, with the diastolic phase end point subtracted). These features showed a marked influence on model predictions in SHAP analyses, underscoring their importance in identifying elevated CVP. Among the top 20 most influential features, 12 were ABP-derived and 8 were PPG-derived (see Fig. 6 and Table 2); 8 were based on mean values and 12 on measures of standard deviation.

Discussion

Our study suggests that the LightGBM model gives the best overall classification performance for this set of combined PPG and ABP features, when all outcome measures are considered together, although both XGBoost and SVC have higher AUROC values and XGBoost, MLP and SVC all have higher AUPRC values. However, LightGBM has the best accuracy, sensitivity, specificity, precession, and F1 score of all the models. The success of the LightGBM and to a lesser extent of the XGBoost over the other models, may be indictive of significant non-linearity in the data as these kinds of models are known to handle non-linearity at scale better than MLP or SVC, with LightGBM most suited to larger data sets.

For LightGBM both precision and sensitivity are greater than 0.8, with precision 0.021 greater than sensitivity. The F1 score represents these two metrics symmetrically in a single parameter and is also greater than 0.8 for this model. However, we note that in the context of identifying elevated CVP, using surrogate measures such as PPG and ABP might best be approached as a triage for deciding whether a more invasive exploration is warranted. It may thus be preferable to prioritize sensitivity over precision (i.e. minimizing false negatives at the cost of accepting a somewhat higher level of false positives). For the LightGBM model chosen here, the more general F_β score with $\beta = 2$, gives sensitivity twice the weight of precision and for our implementation is still >0.8 although 0.05 lower than the F1 score. No other model in our study had an F2 score above 0.8. Further exploration of LightGBM behavior, either with a modified cost function during model training or a reduced threshold for classification may be an interesting future study to optimize the sensitivity-precision balance for clinical settings.

Because the decision-making process of ML models is often described as a “black box” [63], we used SHAP to interpret the predictions of the best-performing classifier (LightGBM). We observe that within the 20 most influential features, 6 of the 8 mean-based features come from the ABP signal whereas the 12 standard deviation-based features are equally divided between those from the PPG and ABP waveforms suggesting that for ABP the both the absolute values and the cycle-to-cycle variation are influential, whereas for PPG the effect of its variation has more impact on the classification. For PPG, the SHAP summary plot indicates that in 4 out of 6 standard deviation-based features, low values tended to contribute to decisions of elevated CVP suggesting that a reduction in cycle-to-cycle variation of waveform morphology is typically predictive of elevated CVP. For ABP waveforms the reverse is true with 5 out of 6 features where high variability is predictive of elevated CVP. For mean values of ABP features, in 4 out of 6 feature low values are predictive of elevated CVP. Many features show patterns in the SHAP summary plot indicative of non-linearity, suggesting that the model output relies on significant interaction between features.

Shelley et al. [21] demonstrated that venous pulsations of central venous origin can cause high variability in the diastolic phase of the PPG waveform, and that venous waveforms can substantially enlarge the diastolic portion of the PPG signal, sometimes contributing up to 40% of the total pulse amplitude [24]. Consistent with these observations, seven of the eight PPG-derived features ranked among the top 20 features overall incorporated information from the diastolic phase of the PPG waveform (see Fig. 6 and Table 2). ABP waveforms provide continuous beat-to-beat blood pressure measurements and deeper insight into overall hemodynamic status [64], supporting prediction of hypo- or hyper-tensive episodes [52] and estimation of cardiac output [39,65]. Furthermore, Mulder et al. [66] showed that ABP waveform morphology changes with preload, contractility, and afterload. Additionally, previous studies have demonstrated a relationship between ABP and CVP waveforms [67,68]; thus, ABP derived features may indirectly capture physiological changes associated with CVP. In this study, we found that ABP waveform features, in combination with PPG-derived features, contributed to the identification of patients with elevated CVP, with 8 of the top 10 most influential features originating from the ABP signal.

This study design has several limitations. First, we trained and tested our ML models on a single-center dataset (MLORD); external validation in larger, multicenter cohorts is needed to assess model generalizability. Second, our analysis focused on features from PPG and ABP waveforms; incorporating clinically relevant features from additional physiological signals, such as non-invasive ECG, may further improve model performance. Third, we did not investigate how PPG recording site (e.g. finger, wrist, forearm, or ear) influences the ability of PPG features to identify elevated CVP; future studies should explore whether

integrating site-specific PPG measurements with ABP waveform features enhances performance and generalizability. Fourth, although PPG is entirely noninvasive, conventional continuous ABP monitoring is invasive and requires arterial catheterization, which carries a small but non-negligible risk of complications. Future work should therefore investigate whether ML models developed using only non-invasive physiological signals - including PPG, ECG, and non-invasively acquired ABP waveforms from continuous ABP monitoring devices, - can achieve comparable performance.

Conclusions

In this study, we evaluated multiple ML models that used combined PPG and ABP waveform features to identify patients with elevated CVP, leveraging the large perioperative MLORD dataset. Among the evaluated models, LightGBM demonstrated the strongest and most balanced performance, achieving a mean AUROC of 0.835 (SD 0.042; 95% CI: 0.749–0.916) and mean AUPRC of 0.841 (SD 0.051; 95% CI: 0.739-0.938). These preliminary results are encouraging and provide a foundation for minimally invasive CVP assessment, but further validation in larger and more diverse multicenter cohorts is needed to confirm the model's generalizability and real-world applicability.

Acknowledgements Not applicable.

Author Contributions R.P. contributed to study design, data analysis, conceptualization, and manuscript preparation. W.R. contributed to preparation, review, and editing of the manuscript. A.R. and J.N.C. contributed to study design and review & editing of the manuscript. A.B. contributed to study design, supervision of the study, review & editing of the manuscript, and conceptualization. M.C. contributed to study design, supervision of the study, review & editing of the manuscript, funding acquisition, and conceptualization. All authors have read and approved the final version of the manuscript.

Funding This work was supported by the National Institutes of Health (NIH): R01EB029751 and R01HL144692.

Data Availability The interested parties may reach out to the first author at (rpal@mednet.ucla.edu) or the corresponding author at (mcannesson@mednet.ucla.edu) to request access to the MLORD dataset and the PPG and ABP waveform featurization tool.

Declarations

Ethics approval and consent to participate This study used the existing, fully de-identified MLORD waveform dataset, which was originally approved by the University of California Los Angeles (UCLA) Institutional Review Board (IRB No. 19-000354). Informed consent was not required as the study involved secondary analysis of a fully de-identified waveform dataset.

Competing interests Dr. Cannesson is a consultant for Edwards Lifesciences and Masimo Corp, and has funded research from Edwards Lifesciences and Masimo Corp. He is also the founder of Sironis and Perceptive Medical and he owns patents and receives royalties for closed loop hemodynamic management technologies that have been licensed to Edwards Lifesciences. All the remaining authors declare no conflict of interest.

Consent for Publication All authors have consented to publication.

Clinical Trial Number Not applicable.

References

1. Roger, C., Muller, L., Riou, B. et al. Comparison of different techniques of central venous pressure measurement in mechanically ventilated critically ill patients. *British Journal of Anaesthesia* **118**, 223-31 (2017).
2. Su, L., Pan, P., Li, D. et al. Central venous pressure (CVP) reduction associated with higher cardiac output (CO) favors good prognosis of circulatory shock: a single-center, retrospective cohort study. *Frontiers in medicine* **6**, 216 (2019).
3. Moinadini, S., Tajoddimi, S. & Hedayat, A.A. Prediction of the central venous pressure in trauma patients on the basis of non-invasive parameters using artificial neural network. *Hong Kong Journal of Emergency Medicine* **28**, 152-164 (2021).
4. Oh, C., Noh, C., Hong, B. et al. Is measurement of central venous pressure required to estimate systemic vascular resistance? A retrospective cohort study. *BMC Anesthesiology* **21**, 310 (2021).
5. Reems, M.M. & Aumann, M. Central venous pressure: principles measurement, and interpretation. *Compendium continuing education for veterinarians* **34** (2012).
6. Zamboni, P., Malagoni, A.M., Menegatti, E. et al. Central venous pressure estimation from ultrasound assessment of the jugular venous pulse. *PLOS ONE* **15**, e0240057 (2020).
7. Backer, D.D. & Vincent, J.L. Should we measure the central venous pressure to guide fluid management? Ten answer to 10 questions. *Critical care* **22**, 43 (2018).
8. Donald, P.L., Fujino, M., Waldman, B. & Miles, L.F. Measurement and interpretation of central venous pressure: a narrative review. *Anaesthesia* **80**, 1093-1102 (2025).
9. Gilbert, M. Central venous pressure and pulmonary artery pressure monitoring. *Anaesthesia & Intensice Care Medicine*

16, 119-123 (2015).
10. Pittman, J.A.L., Ping, J.S. & Mark, J.B. Arterial and venous pressure monitoring. *International Anesthesiology Clinics* **42**, 13-30 (2004).
11. Loh, H.W., Xu, S., Faust, O. et al. Application of photoplethysmography signals for healthcare systems: An in-depth review. *Computer Methods and Programs in Biomedicine* **216**, 106677 (2022).
12. Esper, S. A. & Pinsky, M. R. Arterial waveform analysis. *Best. Pract. Res. Clin. Anaesthesiol* **28**, 363–380 (2014).
13. Cheng, J. *et al.* Prediction of arterial blood pressure waveforms from photoplethysmogram signals via fully convolutional neural networks. *Comput Biol Med* **138**, 104877 (2021).
14. Yoon, D., Jang, J.H., Choi, B.J. et al. Discovering hidden information in biosignals from patients using artificial intelligence. *Korean Journal of Anesthesiology* **73**, 275-284 (2020).
15. Almarshad, M.A., Islam, M.S., Ahmadi, S.A. & Bahammam, A.S. Diagnostic features and potential applications of PPG signal in healthcare: a systematic review. *Healthcare* **10**, 547 (2022).
16. Park, J., Seok, H.S., Kim & S.S., Shin, H. Photoplethysmogram analysis and applications: an integrative review. *Frontiers in physiology* **12**, 808451 (2022).
17. Hajj, C.E. & Kyriacou, P.A. A review of machine learning techniques in photoplethysmography for the non-invasive cuff-less measurement of blood pressure. *Biomedical signal processing and control* **58**, 101870 (2020).
18. Goda, M.A., Charlton, P.H. & Behar, J.A. pyPPG: a python toolbox for comprehensive photoplethysmography signal analysis. *Physiological measurement* **45**, 045001 (2023).
19. Ferizoli, R., Karimpour, P., May, J.M. & Kyriacou, P.A. Arterial stiffness assessment using PPG feature extraction and significance testing in an in vito cardiovascular system. *Scientific reports* **14**, (2024).
20. Charlton, P.H., Pilt, K. & Kyriacou, P.A. Establishing best practices in photoplethysmography signal acquisition and processing. *Physiological measurement* **43**, 050301 (2022).
21. Shelley, K.H., Dickstein, M. & Shulman, S.M. The detection of peripheral venous pulsation using the pulse oximeter as a plethysmograph. *Journal of clinical monitoring* **9**, 283-287 (1993).
22. Hickey, M., Phillips, J.P. & Kyriacou, P.A. The effect of vascular changes on the photoplethysmographic signal at different hand elevations. *Physiol Meas.* **36**, 425-440 (2015).
23. Aleong, E.F. & Chatzizisis, Y.S. Forehead Venous Pulsations in Severe Tricuspid Regurgitation. *N Engl J Med.* **393**, e33 (2025).
24. Fine, J., Branan, K. L., Rodriguez, A. J., Boonya-ananta, T., Ajmal, Ramella-Roman, J. C., McShane, M. J. & Cote, G. L. Sources of Inaccuracy in Photoplethysmography for Continuous Cardiovascular Monitoring. *Biosensors* **11**, 126 (2021).
25. Sami, H.M., Kleinman, B.S. & Lonchyna, V.A. Central venous pulsations associated with a falsely low oxygen saturation measured by pulse oximetry. *J Clin Monit.* **7**, 309-312 (1991).
26. Shelley, K.H., Tamai, D., Jablonka, D., Gesquiere, M., Stout, R.G. & Silverman, D.G. The effect of venous pulsation on the forehead pulse oximeter wave form as a possible source of error in Spo2 calculation. *Anesth Analg.* **100**, 743-747 (2005).
27. Lopez, I.G. & Villegas, E.R. Extracting the jugular venous pulse from anterior neck contact photoplethysmography. *Scientific reports* **10**, 3466 (2020).
28. Lamia B, Chemla D, Richard C, Teboul JL. Clinical review: interpretation of arterial pressure wave in shock states. *Crit Care.* 2005;9(6):601-6. doi: 10.1186/cc3891. Epub 2005 Oct 26. PMID: 16356245; PMCID: PMC1414028.
29. Michard F. Changes in arterial pressure during mechanical ventilation. *Anesthesiology.* 2005 Aug;103(2):419-28;
30. Teboul JL, Monnet X, Chemla D, Michard F. Arterial Pulse Pressure Variation with Mechanical Ventilation. *Am J Respir Crit Care Med.* 2019 Jan 1;199(1):22-31.
31. Marik PE, Cavallazzi R, Vasu T, Hirani A. Dynamic changes in arterial waveform derived variables and fluid responsiveness in mechanically ventilated patients: a systematic review of the literature. *Crit Care Med.* 2009 Sep;37(9):2642-7.
32. Petit M, Vieillard-Baron A. Ventricular interdependence in critically ill patients: from physiology to bedside. *Front Physiol.* 2023 Aug 8;14:1232340.
33. Bove AA, Santamore WP. Ventricular interdependence. *Prog Cardiovasc Dis.* 1981 Mar-Apr;23(5):365-88.
34. Naeije R, Badagliacca R. The overloaded right heart and ventricular interdependence. *Cardiovasc Res.* 2017 Oct 1;113(12):1474-1485
35. Alastruey J, Charlton PH, Bikia V, Paliakaite B, Hametner B, Bruno RM, Mulder MP, Vennin S, Piskin S, Khir AW, Guala A, Mayer CC, Mynard J, Hughes AD, Segers P, Westerhof BE. Arterial pulse wave modeling and analysis for vascular-age studies: a review from VascAgeNet. *Am J Physiol Heart Circ Physiol.* 2023 Jul 1;325(1):H1-H29.
36. Scheer B, Perel A, Pfeiffer UJ. Clinical review: complications and risk factors of peripheral arterial catheters used for haemodynamic monitoring in anaesthesia and intensive care medicine. *Crit Care.* 2002 Jun;6(3):199-204.

37. McGee DC, Gould MK. Preventing complications of central venous catheterization. *N Engl J Med.* 2003 Mar 20;348(12):1123-33.
38. Pal, R., Rudas, A., Kim, S. et al. A signal processing tool for extracting features from arterial blood pressure and photoplethysmography waveforms. In 46th Annual International Conference of the IEEE Engineering in Medicine and Biology Society (EMBC, 2024).
39. Pal, R., Rudas, A., Williams, T. et al. Feature extraction tool using temporal landmarks in arterial blood pressure and photoplethysmography waveforms. *npj Cardiovasc Health* **2**, 57 (2025).
40. Ke, G., Meng, Q., Finley, T. et al. LightGBM: a highly efficient gradient boosting decision tree. In 31st Conference on Neural Information Processing Systems (NeurIPS, 2017).
41. Chen, T. & Guestrin, C. XGBoost: a scalable tree boosting system. *In Proc. 22nd ACM SIGKDD International Conference on Knowledge Discovery and Data Mining* 785–794 (ACM, 2016).
42. Breimann, L. Random forests. *Mach. Learn.* **45**, 5–32 (2001).
43. Nhat-Duc, H. & Van-Duc, T. Comparison of histogram-based gradient boosting classification machine, random Forest, and deep convolutional neural network for pavement raveling severity classification. *Automation in Construction* **148, 1**04767 (2023).
44. Murtagh, F. Multilayer perceptrons and regression for classification. *Neurocomputing* **2**, 183-197 (1991).
45. Zhang, Z. Introduction to machine learning: k-nearest neighbors. *Ann Transl Med* **4**, 218 (2016).
46. Naiem, S., Khedr, A. E., Idrees, A. M. & Marie, M. I. Enhancing the Efficiency of Gaussian Naïve Bayes Machine Learning Classifier in the Detection of DDOS in Cloud Computing. *IEEE Access* **11**, 124597–124608 (2023).
47. Cortes, C., Vapnik, V. Support-vector networks. *Mach Learn* **20**, 273–297 (1995).
48. Cokluk, O. Logistic Regression: Concept and Application. *Educational Sciences: Theory and Practice* **10**, 1397–1407 (2010).
49. Tayade, A., Kumar, S., Shrivastava, A., & Bhallamudi, R. Peripheral arterial disease classification using machine learning and multi-point photoplethysmography. *Computers in Biology and Medicine* **213**, 111835 (2026).
50. Iovino, M., Lazic, I., Loncar-Turukalo, T., Javorka, M., Pernice, R., & Faes, L. Comparison of automatic and physiologically-based feature selection methods for classifying physiological stress using heart rate and pulse rate variability indices. *Physiol. Meas.* **45**, 115004 (2024).
51. Sadad, T. et al. Detection of cardiovascular disease based on ppg signals using machine learning with cloud computing. *Comput. Intell. Neurosci.* **2022**, 1-11 (2022).
52. Hatib, F. et al. Machine-learning algorithm to predict hypotension based on high-fidelity arterial pressure waveform analysis. Anesthesiology 129, 663–674 (2018).
53. Lundberg, S.M. & Lee, S.I. A unified approach to interpreting model predictions. In 31st Conference on Neural Information Processing Systems (NIPS, 2017).
54. Santos, M.R., Guedes, A. & Gendriz, I.S. Shapley additive explanations (SHAP) for efficient feature selection in rolling bearing fault diagnosis. *Machine learning & knowledge extraction* **6**, 316-341 (2024).
55. Kim, S., Kwon, S., Rudas, A., et al. Machine learning of physiologic waveforms and electronic health record data: a large perioperative data set of high-fidelity physiologic waveforms. *Critical care clinics* **39**, 675-687 (2023).
56. Altmann, A., Tolosi, L., Sander, O. & Lengauer, T. Permutation importance: a corrected feature importance measure. *Bioinformatics* **26**, 1340–1347 (2010).
57. Peduzzi, P., Concato, J., Kemper, E., Holford, T.R. & Feinstein, A.R. A simulation study of the number of events per variable in logistic regression analysis. *Journal of Clinical Epidemiology* **49**, 1373-1379 (1996).
58. Huang, J. & Ling, C.X. Using AUC and accuracy in evaluating learning algorithms. *IEEE transactions on knowledge and data engineering* **17**, 299-310 (2005).
59. Hicks, S.A., Strümke, I., Thambawita, V. et al. On evaluation metrics for medical applications of artificial intelligence. *Sci Rep* **12**, 5979 (2022).
60. Efron, B. & Tibshirani, R.J. An Introduction to the Bootstrap. *Chapman & Hall/CRC* (1994).
61. Mohanty, P.K., Francis, S.A.J., Barik, R.K. et al. Leveraging shapley additive explanations for feature selection in ensemble models for diabetes prediction. *Bioengineering* **11**, 1215 (2024).
62. Bobadilla, A.V.P., Schmitt, V., Maier, C.S., et al. Practical guide to SHAP analysis: explaining supervised machine learning model predictions in drug development. *Clin Transi Sci.* **17**, e70056 (2024).
63. Rudin, C. Stop explaining black box machine learning models for high stakes decisions and use interpretable models instead. *Nature machine intelligence* **1**, 206-215 (2019).
64. Nirmalan, M. & Dark, P. M. Broader applications of arterial pressure waveform analysis. Contin. Educ. Anaesth. Crit. Care Pain 14, 285–290 (2014).

65. Saugel, B. et al. Cardiac output estimation using pulse wave analysis physiology, algorithms, and technologies: a narrative review. Br. J. Anaesth. 126, 67–76 (2021).
66. Mulder, M. P. et al. Distinct morphologies of arterial waveforms reveal preload-, contractility-, and afterload-deficient hemodynamic instability: An in silico simulation study. *Physiological Rep.* **10**, (2022).
67. Cretu, I., Tindale, A., Abbod, M., Balachandran, W., Khir, A. W., &Meng, H. A comparison of different methods to maximise signal extraction when using central venous pressure to optimise atrioventricular delay after cardiac surgery. *IJC Heart& Vasculature*. **51**, 101382 (2024).
68. Tindale, A., Cretu, I., Gomez, N., Haynes, R., Meng, H., Mason, M.J., & Francis, D.P. Central venous pressure as a method of optimising atrio-ventricular delay after cardiac surgery. *PLOS ONE.* 20, e0310905 (2025).